Journal of Materials Chemistry A

ROYAL SOCIETY OF CHEMISTRY

COMMUNICATION

View Article Online
View Journal | View Issue

Cite this: *J. Mater. Chem. A*, 2020, **8**, 12291

Received 1st May 2020
Accepted 4th June 2020

DOI: 10.1039/d0ta04551a

rsc.li/materials-a

Synergies between electronic and geometric effects of Mo-doped Au nanoparticles for effective CO_2 electrochemical reduction†

Kun Sun, ‡[ac] Yujin Ji, ‡[de] Yuanyue Liu *[d] and Zhijiang Wang *[ab]

CO_2 electroreduction is developing as a promising technology to solve environmental and energy problems. Alloy catalysts with dissimilar local metal atoms induce geometric and electronic effects that may greatly contribute to their performance. However, the fundamental mechanisms for CO_2 reduction on a bimetallic Au alloy surface are still ambiguous. Here, we report effective CO_2 reduction by the synergies between electronic and geometric effects of Mo-doped Au nanoparticles (MDA NPs). A 97.5% CO faradaic efficiency and 75-fold higher current density than pure Au nanoparticles were achieved at −0.4 V *versus* the reversible hydrogen electrode for MDA NPs with at least 50 h lifetime. Our experimental and theoretical calculation results reveal that the Au surface with increased electron density from Mo can effectively enhance CO_2 activation. Moreover, the intermediate *COOH may be further stabilized by the local Mo atom through additional Mo–O binding to decrease the energy barrier.

The overuse of fossil fuels leads to the energy crisis and severe environmental problems due to the increasing atmospheric CO_2 concentration.[1,2] Reducing CO_2 to produce energy chemicals by using electrochemical methods can theoretically close the anthropogenic carbon cycle.[3,4] The industrial application of CO_2 electroreduction relies on high-performance catalysts with superior selectivity and stability. Researchers worldwide have developed various transition metal catalysts for CO_2 electroreduction under ambient conditions.[5–10] Syngas ($CO + H_2$) is the feedstock for the Fischer–Tropsch process, a technology to produce value-added chemicals and fuels.[11] Therefore, CO production *via* electrochemical CO_2 reduction is the most promising method to address the upcoming energy and environmental problems.[12]

Among the identified metal elements, gold (Au) represents the essential element for catalyzing CO_2 reduction to produce CO with the best selectivity.[13] The high cost and low abundance of Au are the limiting factors preventing its industrial application. Reducing the noble Au usage and improving the specific activity for future applications are of great importance. Hitherto, the preferable catalysts for CO production have often been produced by tuning the microstructure to expose the catalytic surface,[14–17] changing the chemical composition,[10,18,19] and introducing surface strain.[20] However, these previous structural property studies are not sufficient to depict a fundamental protocol at the electronic structure level for CO_2 reduction.

In the pathway of CO production, the adsorbed CO_2 undergoes electron transfer and proton-coupled electron transfer reactions to form *COOH.[21] The sequence of the rate-determining step and the ability to stabilize the *COOH intermediate are the key factors in screening catalysts.[16,22] After the subsequent pathways occur, *CO is formed and desorbed as gaseous CO. For a highly selective CO catalyst, regulating the local electronic environment is vital to facilitate *COOH formation and stabilization and inhibit proton coupling to form H_2. Alloying can introduce electronic and geometric effects by using dissimilar surface atoms with the modified adsorption and stabilization properties of catalysts. Sun *et al.* fabricated Au–Fe core–shell nanoparticles with a jagged surface through surface Fe leaching, thereby showing enhanced mass activity toward CO production.[18] Pd–Au alloys, which are a representative category of catalysts, have a fine-tuned surface atomic structure with improved performance; however, fundamental understanding of geometric and electronic structures of active sites is lacking.[10,23,24] General methods and mechanistic insights

[a]*MIIT Key Laboratory of Critical Materials Technology for New Energy Conversion and Storage, School of Chemistry and Chemical Engineering, Harbin Institute of Technology, Harbin 150001, China. E-mail: wangzhijiang@hit.edu.cn*

[b]*State Key Laboratory of Urban Water Resource and Environment, School of Chemistry and Chemical Engineering, Harbin Institute of Technology, Harbin 150001, China*

[c]*Department of Chemical and Biomolecular Engineering, Rice University, Houston 77005, USA*

[d]*Texas Materials Institute and Department of Mechanical Engineering, The University of Texas at Austin, Austin 78712, USA. E-mail: yuanyue.liu@austin.utexas.edu*

[e]*Institute of Functional Nano & Soft Materials (FUNSOM), Jiangsu Key Laboratory for Carbon-Based Functional Materials & Devices, Soochow University, Suzhou 215123, China*

† Electronic supplementary information (ESI) available. See DOI: 10.1039/d0ta04551a

‡ K. Sun and Y. Ji contributed equally to this work.

should be developed for future industrial application of Au-based electrocatalysts.

Herein, we report a new class of Mo-doped Au nanoparticles (MDA NPs) with highly active, selective, and stable performance to catalyze CO_2 electroreduction to CO under ambient conditions. The maximum CO faradaic efficiency (FE) reached up to 97.5% at −0.4 V *versus* the reversible hydrogen electrode (RHE, all reported potentials are with respect to this reference) with hydrogen evolution totally suppressed which can be maintained for over 50 hours of continuous electrolysis. CO can be detected at an onset potential as low as −0.2 V on the fabricated MDA NPs. Based on density functional theory (DFT) calculations and mechanistic studies, the state-of-the-art performance achieved by MDA NPs stems from the change of the surface electronic structure together with the alloy geometric effect by Mo-doping of Au.

We fabricated highly dispersed MDA NPs by a one-pot solvothermal method at 280 °C using gold acetate ($Au[OOCCH_3]_3$) and molybdenyl acetylacetonate ($[CH_3COCH{=}COCH_3]_2MoO_2$) as metal precursors, 1,2-hexadecanediol as the reducing agent, octyl ether as solvent, and oleic acid and oleyl amine as surfactants. The gold precursor was mixed with a high concentration molybdenum salt solution due to the low solubility of molybdenum in gold.[25] The high-resolution transmission electron microscope images of the MDA NPs (Fig. 1a and b) revealed that the highly dispersed nanoparticles that exhibited uniform sizes of 8.2 ± 0.2 nm in diameter were supported on a carbon black substrate. Fig. 1b shows that the lattice spacing was 0.23 nm for MDA NPs, which is consistent with the face-centered cubic (fcc) Au. The selected-area electron diffraction (SAED) pattern (inset in Fig. 1b) of MDA NPs showed concentric rings composed of bright discrete diffraction spots, revealing the polycrystalline nature of the sample. MDA NP elemental analysis was performed with inductively coupled plasma mass spectrometry, X-ray photoelectron spectroscopy (XPS) and energy-dispersive X-ray spectroscopy (EDS) with an atomic Mo/Au ratio of 8.7% (Table S2†). The compositional distributions of Au and Mo were investigated by elemental mapping using EDS coupled with high-angle annular dark-field scanning transmission electron microscopy (HAADF-STEM). Fig. 1c shows the HAADF-STEM image of a single MDA NP. The EDS elemental maps of Au (Fig. 1d) and Mo (Fig. 1e) as well as their overlapped image (Fig. 1f) were obtained in the same region. These images indicated that Au and Mo atoms were distributed uniformly in the MDA NP. X-ray diffraction measurements were performed to further examine the phase of the MDA NP (Fig. 1g). The diffraction peaks were attributed to the Au (fcc) structure, and no separate diffraction peaks for Mo species can be observed, indicating that no large clusters of the Mo phases existed, and the Mo atoms were mixed in the Au lattice.

XPS measurements of the samples were performed to investigate the electronic properties. The Au 4f and Mo 3d spectra of the MDA NP catalyst indicated the presence of Au and Mo elements in the sample. Fig. 2a shows that the peaks of MDA NPs and Au NPs at the binding energy of about 84 eV can be assigned to metallic gold. Upon MDA NP formation, the binding energy for Au of MDA NPs (83.9 eV) was decreased by 0.1 eV as compared with that of pure Au NPs (84.0 eV). This finding indicated that the electron density of Au increased in the MDA NP, which is in good agreement with the electronegativity considerations between Au and Mo. Thus, charge transfer may occur between Au and Mo in MDA NPs to achieve higher electron density of the Au in MDA NPs compared with its counterpart, pure Au NPs. Fig. 2b shows that Mo of MDA NPs comprises three spin–orbit split components corresponding to metallic Mo and oxidized Mo species including Mo^{4+} and Mo^{6+}, which is also in agreement with previous noble-metal alloys.[26,27] The Mo 3d spectrum for MDA NPs after CO_2 electroreduction (Fig. S11†)

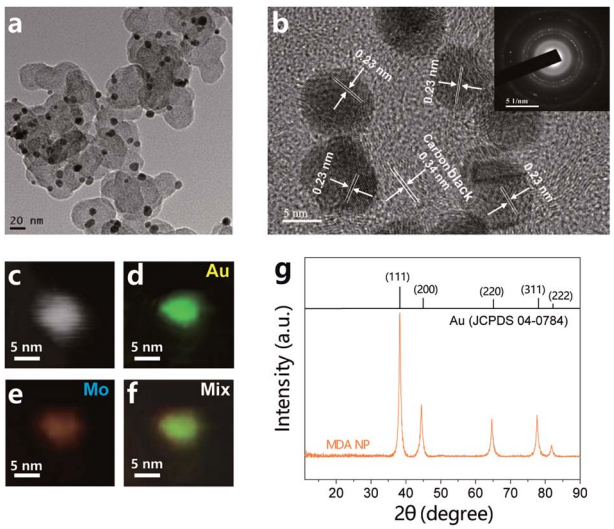

Fig. 1 (a) TEM image of MDA NPs. (b) HRTEM image of MDA NPs loaded on carbon black. Inset: SAED pattern. HAADF-STEM images of (c) a single MDA NP and its corresponding EDS maps of (d) Au and (e) Mo and (f) their overlapped image. (g) X-ray diffraction patterns.

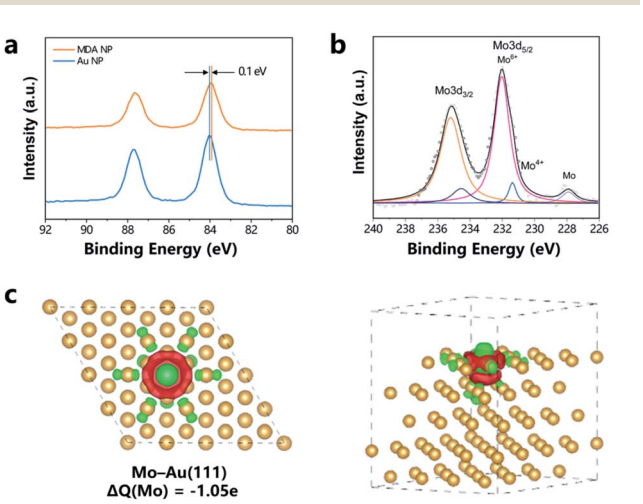

Fig. 2 (a) Au 4f XPS spectra of MDA NPs and Au NPs. (b) Mo 3d XPS spectra of MDA NPs. (c) (Top and side views) charge density difference of Mo-doped Au(111). The green and red colors represent the charge depletion and accumulation areas, respectively. (The isosurface value is set to 0.002 e).

reveals an increased ratio of $Mo^0/Mo^{\delta+}$ indicating the formation of metallic Mo^0 on the particle surface during the reaction, while Mo species inside the nanoparticle still exhibit mixed chemical states. The surface of MDA NPs is occupied by the Au(111) plane based on HRTEM and XRD analysis. We then conducted DFT calculations to investigate the Mo-doping effect on CO_2 reduction and construct Mo-doped Au(111) and pristine Au(111) models to represent the MDA NP and Au NP in the experiment, respectively. Fig. 2c shows that the introduction of the Mo atom was energetically favorable for doping into the Au(111) surface lattice and transfer the electrons to the surrounding Au atoms. According to quantitative Bader charge analysis, the net charge transfer from Mo to Au was 1.05 e, which is in good agreement with the XPS data and also confirms the electron donor role of surface Mo.

We conducted the CO_2 reduction reaction at various applied potentials in 0.5 M $KHCO_3$ solution using MDA NPs and pure Au NPs to evaluate the contribution in catalytic performance by Mo-doping of Au. Au NPs exhibited a similar shape (Fig. S1†) and particle size distribution (Fig. S7†) to MDA NPs to rule out the influence of the particle size and shape.[28,29] CO and H_2 were the only gas products detected on both catalysts from −0.2 V to −1.0 V. Shown in Fig. 3a are linear sweep voltammetry curves of MDA NPs and Au NPs for CO_2 electrolysis. MDA NPs exhibit higher current density than Au NPs. Fig. 3b shows the FE for CO production in which the MDA NPs yielded the highest FE for CO production compared to Au NPs at all tested potentials. When MDA NPs were employed, the onset potential of CO production was at −0.2 V with a considerable amount of CO production, which was only 0.09 V below the theoretical equilibrium potential of CO_2/CO (−0.11 V). The highest FE reached 97.5% at −0.4 V with the competing HER completely suppressed, thus representing the best performance for CO_2 electroreduction among the reported Au-based catalysts at the same potential (Table S1†). For pure Au NPs, the onset potential was −0.4 V with a 0.2 V higher overpotential than MDA NPs to actuate the CO_2 reduction. Moreover, the current density for CO production by Au NPs was only 0.15 mA cm^{-2} at −0.4 V, which was nearly 75-fold smaller than that of MDA NPs (11.22 mA cm^{-2}) at the same potential (Fig. 3c). These results show that MDA NPs are an outstanding catalyst for CO_2 conversion into CO by substantially suppressing the H_2 evolution reaction.

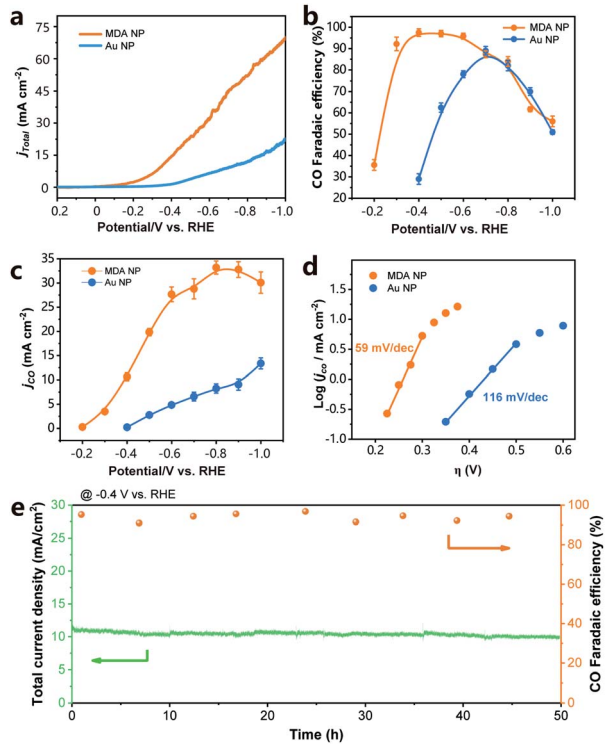

Fig. 3 (a) Linear sweep voltammetry curves of MDA NPs and Au NPs in CO_2-saturated 0.5 M $KHCO_3$ solution. (b) Faradaic efficiencies for CO production by MDA NPs and Au NPs. (c) Current densities for CO production by MDA NPs and Au NPs. (d) Tafel plots of MDA NPs and Au NPs. (e) Catalytic stability test of MDA NPs.

Long-term electrocatalysis was performed at −0.4 V to test the operational stability of the MDA NP. Fig. 3e shows that the MDA NP catalyst possesses a relatively stable current density of ~10.9 mA cm^{-2} toward CO formation with a FE of ~96% over 50 h. The current density and selectivity of Au NPs dropped dramatically during the 10 h electrolysis at −0.7 V, indicating an inferior surface stability compared with MDA NPs (Fig. S4†). Furthermore, the electrochemical surface area (ECSA) of MDA NPs after 50 h of electrocatalysis remains at 95% compared with that before electrolysis, whereas only 20% ECSA remained after 10 h of reaction for Au NPs (Fig. S6†). Thus, the MDA NP shows superior selectivity and long-term stability for CO_2 reduction. Moreover, the area-based catalytic performance based on the ECSA in Fig. S8† provides insight that the active sites in MDA NPs can be further increased by the geometric effect of Mo-doping to possess a larger active surface area and specific activity compared with Au NPs.

We subsequently employed Tafel analysis (Fig. 3d) to explore the kinetic mechanism of CO_2 reduction on MDA NPs and Au NPs. Mo-doping affects the mechanistic pathway during CO_2 electroreduction. A Tafel slope of 116 mV dec^{-1} was observed for Au NPs, implying that the single electron transfer to CO_2 to form surface-adsorbed $CO_2^{\bullet-}$ is the rate-determining step in the whole reaction. By contrast, the Tafel slope for MDA NPs was 59 mV dec^{-1} at relatively low overpotentials, indicating a fast one-electron transfer to the CO_2 molecule as a pre-equilibrating step before the subsequent rate-limiting step.[16,30] The charge transfer from Mo to Au leads to an electron rich surface of MDA NPs that can effectively promote the fast electron transfer to the CO_2 molecule as a fast pre-equilibrium step before the rate-determining step. These results prove that the Mo doped in Au can change the reaction pathway by the formation of electron rich active sites to further improve the catalytic activity, and this finding is in agreement with previous literature.[31,32]

The CO_2 reduction on MDA NPs and Au NPs was elucidated using DFT calculations. For the two-electron pathway for CO_2 reduction to CO in Fig. 4a, the formation steps of *COOH, namely, the first protonation step of CO_2 reduction, corresponds to the electrochemical potential-determining step (PDS), which limits the following CO generation. The free energy barrier at the PDS decreased from 1.15 eV for Au(111) to

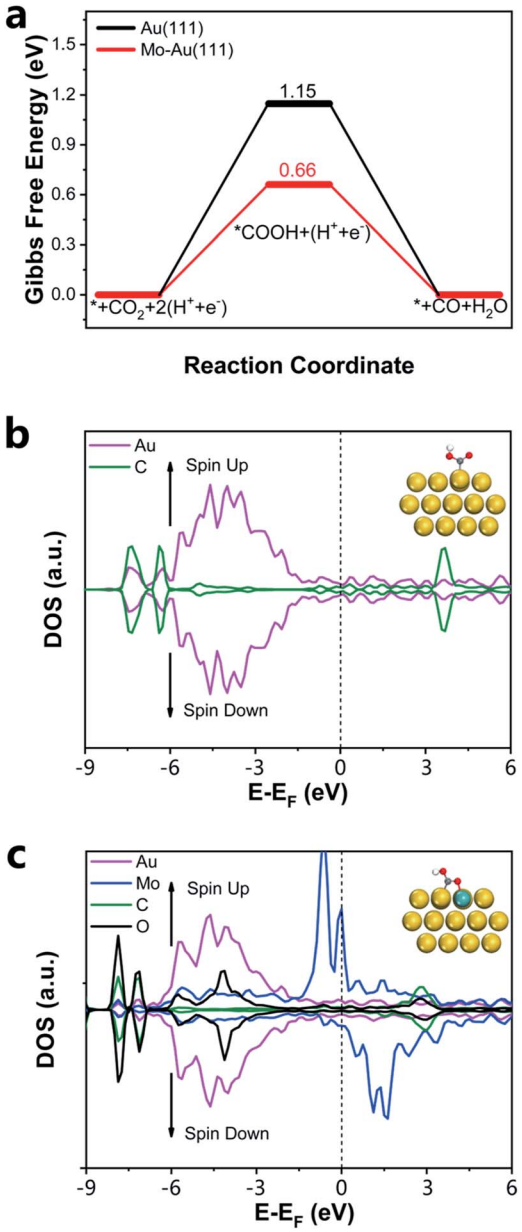

Fig. 4 (a) Free energy diagram of CO_2 reduction on Mo-doped Au(111) and Au(111). Projected density of states analysis of *COOH on (b) Au NPs and (c) MDA NPs. Insets show the optimized binding geometries.

0.68 eV for Mo-doped Au(111), clearly suggesting that the formation of *COOH is highly favorable on the MDA NP. The dopant Mo atom and surrounding Au atoms served as synergetic catalytic sites, in which both the C–Au and O–Mo binding modes are responsible for stabilizing *COOH when compared with the pristine Au(111) surface. Comparison of the projected density of states (Fig. 4b and c) also indicated that except for the electron density overlap in the energy range below −6 eV for C–Au binding modes, O–Mo binding states were observed in the energy range from −6.0 eV to the Fermi level for Mo-doped Au(111). This result implies that the interaction between Mo and *COOH on the Mo-doped Au surface through an additional Mo–O binding can further improve the thermodynamic stability of the *COOH intermediate compared with that on the pure Au surface. Thus, obtaining a low energy barrier for CO_2 reduction using MDA NPs is reasonable to improve the catalytic performance. Furthermore, we also simulated CO_2 reduction on Au(110) and Au(322) surfaces accordingly as shown in Fig. S12 and S13.† It was found that the CO_2 reduction activity on the stepped surfaces is higher than that on Au(111) due to more exposed unsaturated atoms around the stepped sites, and the Mo-doping effect further stabilized the adsorption of the intermediate *COOH, which results in the second protonation process as the potential-limiting step. Meanwhile, we also want to stress that Au(111) had the lowest surface energy, indicating that the Au(111) surface is a dominant exposed surface[33] for Au nanoparticles although the stepped (110) and (322) surfaces are more suitable for CO_2 reduction. Mo-doping on such high energy surfaces could destroy the intrinsic electronic structure and degrade their original high-performances. By comparison, the Mo-doping effect is helpful for improving CO_2 reduction on the Au(111) surface. Therefore, Mo-doping on Au to improve activity exhibits a dependence on the crystal surface, which also confirms the dominating role of Au(111) planes on the MDA NP surface to achieve an enhanced activity compared to Au NPs.

Conclusions

In summary, a highly active and stable MDA NP for CO_2 reduction was synthesized using a solvothermal method. The charge transfer occurred between two elements by introducing Mo into Au to form electron rich Au sites near Mo atoms. For MDA NPs, an impressive CO FE of 97.5% was achieved at −0.4 V together with a 75-fold higher partial current density *versus* Au NPs for at least 50 h. The improved performance originates from the increased electron density of Au in MDA NPs to provide extra affinity for CO_2 activation compared with that in the pristine Au surface. Theoretical calculations also revealed that Mo can help stabilize the *COOH intermediate through an additional Mo–O binding to reduce the energy barrier. These results show that the synergies between the electronic and geometric effects can improve the CO_2 reduction performance for the catalyst and thus provide fundamental mechanism insights into alloy electrocatalysts.

Conflicts of interest

The authors declare no conflict of interest.

Acknowledgements

Z. Wang acknowledges financial support from the National Natural Science Foundation of China (No. 51572062). K. Sun is thankful to the China Scholarship Council for providing a scholarship (201906120349). Y. L. acknowledges the support by the National Science Foundation (Grant No. 1900039) and the Welch Foundation (Grant No. F-1959-20180324). The calculations were performed using computational resources at (1) the National Renewable Energy Lab (sponsored by the DOE's Office of EERE), (2) the Extreme Science and Engineering

Discovery Environment (XSEDE) through allocation TG-CHE190065, (3) the Center for Nanoscale Materials (a DOE Office of Science user facility supported under Contract No. DE-AC02-06CH11357) at the Argonne National Lab, and (4) the Center for Nanophase Materials Sciences (a DOE Office of Science user facility) at the Oak Ridge National Lab.

Notes and references

1 D. R. Feldman, W. D. Collins, P. J. Gero, M. S. Torn, E. J. Mlawer and T. R. Shippert, *Nature*, 2015, **519**, 339–343.
2 S. Chu, Y. Cui and N. Liu, *Nat. Mater.*, 2016, **16**, 16–22.
3 G. A. Olah, G. K. Prakash and A. Goeppert, *J. Am. Chem. Soc.*, 2011, **133**, 12881–12898.
4 A. Goeppert, M. Czaun, J. P. Jones, G. K. Surya Prakash and G. A. Olah, *Chem. Soc. Rev.*, 2014, **43**, 7995–8048.
5 S. Gao, Y. Lin, X. Jiao, Y. Sun, Q. Luo, W. Zhang, D. Li, J. Yang and Y. Xie, *Nature*, 2016, **529**, 68–71.
6 K. Sun, L. Wu, W. Qin, J. Zhou, Y. Hu, Z. Jiang, B. Shen and Z. Wang, *J. Mater. Chem. A*, 2016, **4**, 12616–12623.
7 C. G. Morales-Guio, E. R. Cave, S. A. Nitopi, J. T. Feaster, L. Wang, K. P. Kuhl, A. Jackson, N. C. Johnson, D. N. Abram, T. Hatsukade, C. Hahn and T. F. Jaramillo, *Nat. Catal.*, 2018, **1**, 764–771.
8 Z. Wang, L. Wu, K. Sun, T. Chen, Z. Jiang, T. Cheng and W. A. Goddard 3rd, *J. Phys. Chem. Lett.*, 2018, **9**, 3057–3061.
9 D. D. Zhu, J. L. Liu and S. Z. Qiao, *Adv. Mater.*, 2016, **28**, 3423–3452.
10 S. Zhu, Q. Wang, X. Qin, M. Gu, R. Tao, B. P. Lee, L. Zhang, Y. Yao, T. Li and M. Shao, *Adv. Energy Mater.*, 2018, **8**, 1802238.
11 A. Y. Khodakov, W. Chu and P. Fongarland, *Chem. Rev.*, 2007, **107**, 1692–1744.
12 Q. Lu and F. Jiao, *Nano Energy*, 2016, **29**, 439–456.
13 J. Qiao, Y. Liu, F. Hong and J. Zhang, *Chem. Soc. Rev.*, 2014, **43**, 631–675.
14 A. J. Welch, J. S. DuChene, G. Tagliabue, A. Davoyan, W.-H. Cheng and H. A. Atwater, *ACS Appl. Energy Mater.*, 2018, **2**, 164–170.
15 N. T. Nesbitt, M. Ma, B. J. Trześniewski, S. Jaszewski, F. Tafti, M. J. Burns, W. A. Smith and M. J. Naughton, *J. Phys. Chem. C*, 2018, **122**, 10006–10016.
16 Y. Chen, C. W. Li and M. W. Kanan, *J. Am. Chem. Soc.*, 2012, **134**, 19969–19972.
17 Z. Cao, S. B. Zacate, X. Sun, J. Liu, E. M. Hale, W. P. Carson, S. B. Tyndall, J. Xu, X. Liu, X. Liu, C. Song, J. H. Luo, M. J. Cheng, X. Wen and W. Liu, *Angew. Chem.*, 2018, **57**, 12675–12679.
18 K. Sun, T. Cheng, L. Wu, Y. Hu, J. Zhou, A. Maclennan, Z. Jiang, Y. Gao, W. A. Goddard 3rd and Z. Wang, *J. Am. Chem. Soc.*, 2017, **139**, 15608–15611.
19 D. Kim, J. Resasco, Y. Yu, A. M. Asiri and P. Yang, *Nat. Commun.*, 2014, **5**, 4948.
20 E. L. Clark, C. Hahn, T. F. Jaramillo and A. T. Bell, *J. Am. Chem. Soc.*, 2017, **139**, 15848–15857.
21 R. Kortlever, J. Shen, K. J. P. Schouten, F. Calle-Vallejo and M. T. M. Koper, *J. Phys. Chem. Lett.*, 2015, **6**, 4073–4082.
22 N. J. Firet and W. A. Smith, *ACS Catal.*, 2017, **7**, 606–612.
23 X. Yuan, L. Zhang, L. Li, H. Dong, S. Chen, W. Zhu, C. Hu, W. Deng, Z.-J. Zhao and J. Gong, *J. Am. Chem. Soc.*, 2019, **141**, 4791–4794.
24 Y. Wang, L. Cao, N. J. Libretto, X. Li, C. Li, Y. Wan, C. He, J. Lee, J. Gregg, H. Zong, D. Su, J. T. Miller, T. Mueller and C. Wang, *J. Am. Chem. Soc.*, 2019, **141**, 16635–16642.
25 T. B. Massalski, H. Okamoto, P. R. Subramanian and L. Kacprzak, *Binary Alloy Phase Diagrams*, ASM International, 2nd edn, 1990.
26 Z. Liu, J. E. Hu, Q. Wang, K. Gaskell, A. I. Frenkel, G. S. Jackson and B. Eichhorn, *J. Am. Chem. Soc.*, 2009, **131**, 6924–6925.
27 X. Huang, Z. Zhao, L. Cao, Y. Chen, E. Zhu, Z. Lin, M. Li, A. Yan, A. Zettl, Y. M. Wang, X. Duan, T. Mueller and Y. Huang, *Science*, 2015, **348**, 1230.
28 H. Mistry, R. Reske, Z. Zeng, Z.-J. Zhao, J. Greeley, P. Strasser and B. R. Cuenya, *J. Am. Chem. Soc.*, 2014, **136**, 16473–16476.
29 N. Todoroki, H. Tei, H. Tsurumaki, T. Miyakawa, T. Inoue and T. Wadayama, *ACS Catal.*, 2019, **9**, 1383–1388.
30 M. Ma, B. J. Trześniewski, J. Xie and W. A. Smith, *Angew. Chem., Int. Ed.*, 2016, **55**, 9748–9752.
31 Z. Cao, J. S. Derrick, J. Xu, R. Gao, M. Gong, E. M. Nichols, P. T. Smith, X. Liu, X. Wen, C. Copéret and C. J. Chang, *Angew. Chem., Int. Ed.*, 2018, **57**, 4981–4985.
32 Z. Cao, D. Kim, D. Hong, Y. Yu, J. Xu, S. Lin, X. Wen, E. M. Nichols, K. Jeong, J. A. Reimer, P. Yang and C. J. Chang, *J. Am. Chem. Soc.*, 2016, **138**, 8120–8125.
33 L. Vitos, A. V. Ruban, H. L. Skriver and J. Kollár, *Surf. Sci.*, 1998, **411**, 186–202.